Evaluation of Polymorphism and Charge Transport in BaO-CaO-Ta2O5 Perovskite Phase Diagram Using TOF-neutron and synchrotron X-ray diffraction, Bond-valence method and Impedance Spectroscopy

Complete List of Authors:	Singh, Kalpana; University of Calgary Yang, Hua; Institute of High Energy Physics, Dongguan Institute of Neutron Science Zhang, Zheyu; University of Calgary Avdeev, Maxim; Australian Nuclear Science and Technology Organisation (ANSTO), Australian Centre for Neutron Scattering Huq, Ashfia ; Oak Ridge National Laboratory Wu, Dong-Ying; National Synchrotron Radiation Research Center Lee, Jey-Jau; National Synchrotron Radiation Research Center of Taiwan Kan, Wang Hay; Institute of High Energy Physics, China Spallation Neutron Source Thangadurai, Venkataraman; University of Calgary, Department of Chemistry

Evaluation of Polymorphism and Charge Transport in BaO-CaO-Ta$_2$O$_5$ Perovskite Phase Diagram Using TOF-neutron and synchrotron X-ray diffraction, Bond-valence method and Impedance Spectroscopy

Kalpana Singh[2,#], Hua Yang[1,3,#], Zheyu Zhang[2,#], Maxim Avdeev[4], Ashfia Huq[5], Dong-Ying Wu[6], Jey-Jau Lee[6], Wang Hay Kan[1,*], Venkataraman Thangadurai[2,*]

[1]Dongguan Neutron Science Center, No. 1 Zhongziyuan Road, Dongguan, Guangdong, 523803 China

[2]Department of Chemistry, University of Calgary, Calgary, Alberta, T2N 1N4, Canada

[3]Institute of High Energy Physics, Chinese Academy of Sciences, Beijing 100049, China

[4]Australian Nuclear Science and Technology Organisation (ANSTO), New Illawarra Road, Lucas Heights, New South Wales 2234, Australia

[5]Neutron Scattering Science Division, Oak Ridge National Laboratory, Oak Ridge, Tennessee 37831, United States

[6]National Synchrotron Radiation Research Center, No. 101 Hsin-Ann Rd., Hsinchu 300, Taiwan

[#] These authors contribute equally to this work.

*Email: jianhx@ihep.ac.cn, vthangad@ucalgary.ca

Abstract

Among the alkaline earth-based perovskite oxides, the Ba-based perovskites have superior chemical stability and tunable electrical/catalytic property via chemical substitution/doping. One of the best-known examples is Ba$_3$Ca$_{1.18}$Nb$_{1.82}$O$_{8.73}$ as ceramic proton conductor for all-solid-state steam electrolysis and solid oxide fuel cells (SOFCs). The structural ordering variation is often driven by chemical composition, which directly correlates with their chemical/physical properties. In the present work, we develop a comprehensive functional perovskite-type phase diagram for the Ba-Ca-Ta-O quaternary system Ba$_3$Ca$_{1+x}$Ta$_{2-x}$O$_{9-3x/2}$ ($0 \leq x \leq 0.36$) with a wide chemical composition between 1000 and 1550 ^{o}C, coupled with theoretical calculations to investigate the cationic ordering in the supercells. Furthermore, the impact of cationic clustering on the diffusion pathways of O^{2-} ions were evaluated as a case study. Experimentally, the precise cationic orderings and other structural features are quantitively determined by TOF-neutron and synchrotron X-ray

diffraction analyses. This work provides a comprehensive evaluation about some potential applications of the Ba-Ca-Ta-O quaternary system. The electrochemical impedance data was also systematically studied by impedance spectroscopy genetic programming (ISGP). The electrical conductivity was found to increase from $x = 0$ to $x = 0.27$, and then decrease for end member when $x = 0.36$ due to decrease in mobile charge carrier concentration. Interestingly, in dry air, electrical conductivity was found to increase from $x = 0$ to $x = 0.36$. However, only $Ba_3Ca_{1.18}Ta_{1.82}O_{8.73}$ (BCT18) and $Ba_3Ca_{1.27}Ta_{1.73}O_{8.595}$ (BCT27) were found to show an increasing trend in conductivity in humid atmospheres, and these indicate that the clustering effect was pO_2 dependent.

1. INTRODUCTION

Cationic/anionic conducting metal oxides have a wide range of electrochemical applications, such as steam electrolyzes, fuel cells, sensors, gas separation membranes and electrochromic devices. Over the years, numerous chemical compositions dependent structural types have been investigated with an aim to produce compounds with suitable chemical/physical properties and chemical compatibilities for various practical applications. One of the best known examples are the high temperature proton conductors, namely Y-doped $SrCeO_3$ and $BaMO_3$ (M = Ce, Zr) with a perovskite-type structure, developed by Ishihara and others in the early 1980s.[1] On the contrary, employing these materials in commercialised applications is a great challenge as most of the perovskite-type proton conductors do not meet the combination of practical requirements, such as proton conductivity, stability towards CO_2, and reasonable costs. On the other hand, complex perovskite-type $A_3B'_{1+x}B''_{2-x}O_{9-\delta}$, oxides with A/B-site orderings show high chemical stability under CO_2 and H_2O and reasonably good protonic conductivities at intermediate temperatures (400 - 700 ºC).[2-4] The complex perovskites $Ba_3Ca_{1+x}Nb_{2-x}O_{9-3x/2}$ (BCN), which exhibit good proton conductivity, were one of the best-known examples for this category. Nonetheless, only a handful of complex quaternary perovskites have been reported in the perovskite structure. For the known compounds, the structural or ordering variation are often driven by composition changes, directly impacting the chemical/physical properties. As such, we and others systematically investigated the ordering-dependent transport property of $Ba_3Ca_{1+x}Nb_{2-x}O_{9-\delta}$ as a function of x, and the doped species as a function of temperatures, to understand how to optimize electrical/catalytic property.[2-8]

The crystal radii of the 6-coordinated Ta^{5+} and Nb^{5+}ions (0.78 Å) with O^{2-} ions are identical,[9] but Ta^{5+} ions ($Ta_2O_{5(s)}$ + $10H^+_{(aq)}$ + $10e^-$ ⇆ $2Ta_{(s)}$ +$5H_2O_{(l)}$; -0.752 V vs. Standard

Hydrogen Electrode, S.H.E.) are less reducible than that of Nb^{5+} ions ($Nb_2O_{5(s)} + 10H^+_{(aq)} + 10e^-$

$\leftrightarrows 2Nb_{(s)} + 5H_2O_{(l)}$; -0.601 V vs. S.H.E.).[10] This suggests that the electronic leaking is lower for Ta

compounds and therefore, the isostructural Ta-type analogs might provide superior

chemical/physical stability comparing to their Nb-counterparts. Thangadurai *et al.* showed that

$Li_5La_3M_2O_{12}$ (Nb, Ta) were isostructural but only $Li_5La_3Ta_2O_{12}$ was chemically stable with lithium

molten metal.[11-12] Kan *et al.* recently demonstrated that $Li_{1.3}Ta_{0.3}Mn_{0.4}O_2$ was insoluble with aqua

regia, while $Li_xNb_{0.3}Mn_{0.4}O_2$ ($0 \leq 0 \leq 1.3$) could be dissolved completely in the same medium.[13-15] Filonenko *et al.* observed that the phase transition and melting temperatures were higher for

Ta_2O_5 than Nb_2O_5 for numerous polymorphs.[16] We, therefore, are also interested to develop a

better understanding for the structure-property relationship of the $Ba_3Ca_{1+x}Ta_{2-x}O_{9-\delta}$ as functional

perovskites.

Up to now, the Inorganic Compound Structure Database (ICSD) has collected 93 Ba-M-

Ta-O quaternary perovskite-type metal oxides with a general chemical formula of $Ba_3M_{1+x}Ta_{2-x}O_{9-\delta}$. Although all M^{n+} ions are octahedrally coordinated with O^{2-} ions, their ionic size and charge

are the two main factors to drive them to crystallize into 7 different space groups: *I4/m* (M = Ho^{3+},

Eu^{3+}, Y^{3+}),[17-20] *I12/m1* (M = Bi^{3+}, La^{3+}, Ce^{3+}, Lu^{3+}),[18, 21-23] *P12₁/n1* (M = La^{3+}),[18, 24] *R-3R* (M =

La^{3+}, Bi^{3+}),[18, 21, 25] *P6₃/mmc* (M = Sr^{2+}, Li^+, Cr^{3+}),[26-28] *Fm-3m* (M = Yb^{3+}, Bi^{3+}, Ho^{3+}, Y^{3+}, Ca^{2+},

In^{3+}, Lu^{3+}),[17-18, 24-25, 29-32] *Pm-3m* (M = Mg^{2+}, Co^{2+}, Fe^{2+}, Mn^{2+}, Y^{3+}, Sc^{3+}, Yb^{3+}, Ca^{2+}),[33-37] and *P-3m1* (M = Mg^{2+}, Zn^{2+}, Ca^{2+}, Ni^{2+}, Sr^{2+}).[30, 34, 38-44] Among the above groups, lanthanum ions or

cations with 3+ charge often have a tendency to crystallize into open structures to reduce the

electrostatic interaction, they include *I4/m, I12/m1,* P12₁/n1, *R-3R*, and *P6₃/mmc*.

To design a functional perovskite-type material, one of the key parameters is to create

certain oxide-ion vacancy content δ as a mean to achieve a charge neutrality inside the unit cell.

Additionally, the use of divalent cations, such as Ca^{2+} or Mg^{2+} could be advantageous as the oxide vacancy concentration is proportional to $3x/2$, higher than that of x if M are trivalent species. Comparing to Mg^{2+} ion (-2.7 V vs. S.H.E.), Ca^{2+} ions (-3.02 V vs. S.H.E.) have a larger negative reduction potential, which could provide a wider electrochemical and temperature window for potential applications.[10] As such, we focus on the construction a phase diagram with a divalent Ca ion as a case study where its methodology could be applicable to other divalent or trivalent species.

Over the years, the $BaO-CaO-Ta_2O_5$ system was not well-studied in the past 6 decades. From the ICSD database, only $Ba_3CaTa_2O_9$ and $Ba_3Ca_{1.18}Ta_{1.82}O_{8.73}$ were reported by Galasso *et al.* in 1960 and Irvine *et al.* in 2011,[30, 42] respectively. The structure of $Ba_3CaTa_2O_9$ was cubic with a space group of *Pm-3m*, while $Ba_3Ca_{1.18}Ta_{1.82}O_{8.73}$ was a mixture of *Fm-3m* and *P-3m1* with the corresponding molar ratio of 84:16. The reports of three different space groups for two chemically similar compositions suggested that their solid solution region could be very limited, if existed. Such a situation was not consistent with the well-known $Ba_3Ca_{1+x}Nb_{2-x}O_{9-3x/2}$ where the family of compounds crystallizes into *Fm-3m* for x between 0 and 0.36.[8] Given the fact that the statistical crystal radii of the 6-coordinated Nb^{5+} and Ta^{5+} ions (0.78 Å) with O^{2-} ions are identical, the $Ba_3Ca_{1+x}M_{2-x}O_{9-3x/2}$ (M = Nb and Ta) series are expected to share a similar structural feature. The unexpected results inspired us to conduct a thorough investigation on the heat-treatment process and analyze if any unknown kinetic phase could be found. In fact, the synthesis of $Ba_3CaTa_2O_9$ and $Ba_3Ca_{1.18}Ta_{1.82}O_{8.73}$ was conducted at quite difference temperatures and atmosphere regimes; the former was prepared at 1100 °C under vacuum and the latter was prepared at 1500 °C in air. In this manuscript, we conduct a comprehensive functional perovskite-type phase diagram for the $BaO-CaO-Ta_2O_5$ system for a wide composition between 1000 and 1550 °C. Finally, the bond valence energy landscapes were computed to estimate the diffusion pathways H^+ and O^{2-},[7-8, 14-15,]

[45-48] to evaluate their usefulness in different energy storage and conversion applications[49-52]. To understand the distribution of different cations in the same crystallographically distinct sites, the supercells and their relative energies were also evaluated to understand if cationic clustering may be present. Precise ordering and structural features were quantified by TOF-neutron and synchrotron X-ray diffraction analyses. For the electrical measurement, conventional equivalent circuit modeling (ECM) is used to separate individual electrochemical processes, however situation becomes more difficult to interpret when the relaxation times are similar.[53] In cases, where processes with similar relaxation times are present, deconvolution of semicircles in Nyquist plots through ECM may present similar impedance curves with different fitting models and, thus a meaningful interpretation of the electrochemical processes involved is prevented.[53] Thus, in order to separate individual electrochemical processes meaningfully, impedance spectroscopy genetic programing (ISGP) was employed in current work. [54-56] This work provides a useful comprehensive study to evaluate some potential applications of the $BaO-CaO-Ta_2O_5$ system.

2.   EXPERIMENTAL

2.1 Synthesis. Oxides with nominal formula $Ba_3Ca_{1+x}Ta_{2-x}O_{9-1.5x}$ (x = 0. 0.09, 0.18, 0.27 and 0.36) were synthesized in air through conventional solid-state reaction method. Stoichiometric amounts of $BaCO_3$ (Sigma-Aldrich, 99%), $CaCO_3$ (GFS Chemicals, ACS-grade) and Ta_2O_5 (Alfa Aesar, 99%) were ground and mixed in a ball mill (Fritsch Pulverisette 7) using stabilized zirconia balls for 2 h at 250 rpm, and subsequently 4 h at 200 rpm, both with iso-propanol as the solvent. The dried powders were first heated at 1000 °C for 12 h and ball-milled again under similar conditions. Then the powders were cold pressed into thin pellets by a die (13 mm in diameter) under a load of 10 kN for 5 mins. The pellets were subject to final sintering at 1000, 1100, 1400 and 1550 °C for 24 h in air. The $Ba_3Ca_{1+x}Ta_{2-x}O_{9-1.5x}$ (x = 0. 0.09, 0.18, 0.27 and 0.36) samples, prepared at 1000

°C, were named BCT00-1000, BCT09-1000, BCT18-1000, BCT27-1000 and BCT36-1000. All other samples were named following the same manner.

2.2 Characterization. The crystal structure of all samples was characterized by Bruker D8 ADVANCE (Cu Kα radiation, 45 kV, 40 mA; 2θ = 10 - 90°, 10 s per step) and D2 PHASER (Cu Kα radiation, 30 kV, 10 mA; 10 - 90°, 1 s per step) powder X-ray diffractometers (PXRD) at 2θ = 10 - 80° with steps of 0.02° at room temperature. Synchrotron X-ray diffraction was performed at ambient temperature at 2θ = 3 - 62° with a 2θ step size of 0.01° with a monochromatic X-ray (λ = 1.321 Å) at BL17A1 in the Taiwan Light Source (TLS), National Synchrotron Radiation Research Center (NSRRC). The samples were mounted between Kapton films. Time of flight (TOF) neutron diffraction (ND) data were collected at the Oak Ridge National Laboratory (ORNL) Spallation Neutron Source (SNS) POWGEN beamline using a neutron beam with a center wavelength of 0.8 Å (d-spacing range of 0.2 - 9.0 Å). Conventional Rietveld method using the General Structure Analysis System (GSAS) package with the graphical user interface (EXPGUI) was used to refine the X-ray and neutron data. [57] The background, scale factor, zero (X-ray only), absorption (neutron only), cell parameters, atomic positions, thermal parameters, and profile coefficients for the Pseudo Voigt/Finger, Cox, and Jephcoat (FCJ) asymmetric peak shape function were refined until convergence. The shifted Chebyschev and reciprocal interpolation functions were used to model the background of neutron and X-ray data, respectively. The Ca/Ta distribution was determined in both *P-3m1* and *Fm-3m* phases, using constraints in the refinement program. For *P-3m1* phase, due to the different multiplicity in *1b* and *2d* sites, the change of *2d* site occupancy leads to the change of 1b site occupancy times -2. For *Fm-3m* phase, the change of *2d* site occupancy leads to the change of 1b site occupancy. Such setup was to allow Ca^{2+} and Ta^{5+} ions distribution to change between those sites, while maintaining the overall chemical composition of the sample constant.

Bond valence sum (BVS) mismatch maps and bond valence energy landscapes (BVEL) were calculated using 3DBVSMAPPER, an automatic program developed by Sale and Adveev. [58] The Crystallographic Information Files (cifs) were downloaded from the latest ICSD database or obtained from the Supercell program described below. The cifs, with a space group of *P-3m1*, were extracted from our Rietveld based on both neutron and X-ray data for $Ba_3CaTa_2O_9$. Another hypothetical structure, with a space group of *Fm-3m*, was created for $Ba_3Ca_{1.5}Ta_{1.5}O_{8.25}$ in which Ca^{2+} and Ta^{5+} ions only occupied the *4a* and *4b* sites, respectively. The above two cif files were assumed to have no Ca/Ta mixing to simplify the calculation; the oxidation states of Ba, Ca, Ta and O ions were assumed to be 2+, 2+, 5+ and 2-, respectively, in the structures. The unit cells were divided into grid size of 0.2 along each cell dimension to obtain BVS mismatch in 3 dimensions. BVS mismatch map calculations were performed for H^+ and O^{2-} ions to evaluate if the structures are suitable for different functional applications. BVEL was calculated to see the impact of cationic cluster on the diffusion behavior of O^{2-} ions in the structure.

Supercells were calculated using Supercell V.2.0.2 developed by Okhotnikov and Cadars.[59] The input cifs were first downloaded from the ICSD database with fixed valence states assigned to each atom in the crystallographic distinct sites. The unit cells should be charge-balanced prior to the supercell calculation. The sizes of the investigated supercells were maximized by extending the unit cell along X, Y and Z and were limited only by the maximum number of configurations of 10^{15}.

The morphology and energy dispersive X-ray spectroscopy (EDX) were examined by using a Zeiss Sigma VP Series Scanning Electron Microscope (SEM). The Archimedes method (Mettler Toledo Density Kit) was employed to measure the density (ρ) of BCT pellets at room temperature, and ρ is calculated using the relationship:

$$\rho_{pellet} = \frac{\rho_{solv} M_{Dry}}{M_{sat} - M_{sus}}$$ [1]

where ρ_{solv} is the room temperature density of distilled water (0.997 g/cm^3 at 25 °C), M_{Dry} is the dry weight of pellet, M_{sat} is the water-saturated weight of pellet, and M_{sus} is the suspended weight of the pellet in water.

Electrical transport properties were measured by a Solartron (Model No. 1260; 10 MHz to 0.1 Hz, 100 mV) frequency analyzer in 2-probe setting under air, 3% H_2O/air, and 3% D_2O/air and N_2 between 300 – 800 °C. 3% H_2O/air and 3% D_2O/air atmospheres were obtained by bubbling air at room temperature through water and D_2O, respectively. Prior to the measurement, pellets (~10 mm in diameter, ~ 2mm in thickness) were brush-painted on both sides with gold paste (Heraeus) and cured at 800 °C to provide current collector layers. The electrochemical impedance spectra (EIS) were recorded after the samples were rested for a minimum of 3 h to attain thermal equilibrium. Impedance spectroscopy genetic programing (ISGP) was used to analyse AC impedance data.[60-63] In ISGP, genetic algorithm is utilized in order to find the most suitable distribution function of relaxation times (DFRT). The main benefits of ISGP over equivalent circuit modeling (ECM) for analyzing AC impedance data are: a priori knowledge of the system is not needed, the use of discrepancy-complexity approach can avoid overfitting,[60] and it can eliminate the use filter or Lagrange coefficients for regularization, which can result in either artificial peaks or too smooth solution, as opposed to other DFRT methods. Additionally, analytic function in ISGP easily separates convoluted processes in Nyquist's plots and follows the behavior of each peak separately. The correlation between the measured impedance and distribution function of relaxation times (DFRT) is shown in Equation 2:[61-65]

$$Z(\omega) = R_\infty + R_{pol} \int_{-\infty}^{\infty} \frac{\Gamma(\log(\tau))}{1 + i\omega\tau} d(\log(\tau))$$ [2]

where Z is the impedance, R_∞ is the series resistance, R_{pol} is the total polarization resistance, Γ is the DFRT, τ is the relaxation time, and ω is the angular frequency. DFRT cannot be directly extracted from the measured impedance data from equation 1, as it is an ill-posed inverse problem, and thus advanced numeric technique such as MATLAB is used to run ISGP.[61] Detailed description of ISGP approach can be found in previous reports.[54-56]

3. RESULTS AND DISCUSSION

3.1. Structural analysis. All investigated $Ba_3Ca_{1+x}Ta_{2-x}O_{9-3x/2}$ (x = 0, 0.09, 0.18, 0.27, 0.36) samples were prepared by conventional solid-state method. To understand the temperature-dependent phase formation, the samples were heated at four specific temperatures, namely 1000 °C, 1100 °C, 1400 °C and 1550 °C. A comprehensive phase diagram was created to summarize the presence of *P-3m1* and *Fm-3m* as a function of temperature and off stoichiometry x, as shown in Figure 1. The phase fraction and atomic ordering were quantified by Rietveld refinement on synchrotron X-ray and TOF-neutron data (Figure 2-4 and, Table S1). Our findings reveal that *P-3m1* phase could be obtained at as low as 1000 °C for $Ba_3CaTa_2O_9$; such a crystal structure appears to have a wide range of solid-solution region between x = 0 and 0.36 (Figure 5a). Thermogravimetric analysis (TGA; Figure S1) also showed that a weight loss of ca. 15% was observed from the precursor of all investigated $Ba_3Ca_{1+x}Ta_{2-x}O_{9-3x/2}$ between room temperature and 1000 °C in air, which was in good agreement with the theoretical weight loss attributed by the thermal decomposition of carbonate precursors into the corresponding metal oxides and CO_2. However, our observation for the *P-3m1* phase of $Ba_3CaTa_2O_9$ was not completely consistent with the Galasso *et al.'s* 1960 report in which they observed a mixture of cubic *Pm-3m* phase of $Ba_3CaTa_2O_9$ with a hexagonal phase of $Ba_5Ta_4O_{15}$. In the last part of their report, Galasso *et al.*

expressed concerns about their initial synthetic attempts because they obtained a compound with the same composition as the starting mixture, indicating reproducibility problem in their synthesis and characterization. We suspected that their precursors might not have been properly mixed prior to the heat-treatment process, which lead to obtaining some unwanted kinetically stablized products. Therefore, we specifically optimized our precursor ball-milling mixing procedure in terms of time and revolutions per minute (rpm) parameters, and our synthesis yielded very consistent result as shown below.

Except for $Ba_3CaTa_2O_9$, all the investigated samples prepared at 1000 ^oC have small amount of $BaCO_3$ or $CaCO_3$. Although the TGA measurement indicated that all precursors decomposed completely to form the corresponding *P-3m1* type perovskites, the final products might be susceptible to a reaction with CO_2 in air to form the carbonates. This observation was in good agreement with the work of Saito *et al.* in which they found by TGA analysis that their as-prepared $Ba_2(Zn_{2/3}M_{1/3})_2O_5$ (M = Nb and Ta) contained carbonates. The amount of Ca/Ta disordering was found to be 8.68% for $Ba_3CaTa_2O_9$, increased progressively to 18.79% and 20.01% as x increased further for $Ba_3Ca_{1.09}Ta_{1.91}O_{8.865}$ and $Ba_3Ca_{1.18}Ta_{1.82}O_{8.73}$, respectively. However, as x increased more, the disordering was found to reduce to 12.92% and 9.55% for $Ba_3Ca_{1.27}Ta_{1.73}O_{8.595}$ and $Ba_3Ca_{1.36}Ta_{1.64}O_{8.46}$ (Figure 5b). Such Ca/Ta mixing could reduce the lattice energy of the bulk samples, leading to the decrease in their chemical/physical stability (e.g., with CO_2). As a comparison, we also observed various amount of Ca/Nb disordering in the low temperature synthesized *Fm-3m* phase for $Ba_3Ca_{1+x}Nb_{2-x}O_{9-3x/2}$ ($0 \leq x \leq 0.36$) in our previous study. This room-temperature CO_2 uptake ability is unique and tunable; it could be promising to develop as an effective room temperature CO_2 absorbent for commercial applications.

As temperature increased to 1100 °C and 1400 °C, all investigated $Ba_3Ca_{1+x}Ta_{2-x}O_{9-3x/2}$ (0 < x ≤ 0.36) appeared to be a two-phase mixture of *P-3m1* and *Fm-3m*. The mole fraction of *P-3m1* was higher than that of *Fm-3m* for all samples prepared at 1100 °C, but trend was revered as temperature was increased to 1400 °C (Figure 5c), suggesting that *Fm-3m* could be a more thermodynamic stable phase for the $Ba_3Ca_{1+x}Ta_{2-x}O_{9-3x/2}$ series. One exception is for the chemical composition of $Ba_3CaTa_2O_9$, i.e., only *P-3m1* phase was observed between 1000 °C and 1550 °C, and the Ca/Ta disordering was found to decrease with increasing in temperature. This indicates that both temperature and stoichiometry are critical to control the formation enthalpy (ΔH) of both *P-3m1* and *Fm-3m* phases. At 1550 °C, except for $Ba_3CaTa_2O_9$, all samples could be identified as *Fm-3m* phases, with no Ca/Ta disordering in their structures. This is also confirmed with SEM and EDX images that all samples were quite homogenous in size and shape and the distribution of all elements was very uniform (Figure S2).

3.2. Theoretical calculations for energetically favorable supercell configurations and the diffusion of different mobile species. The main purpose to develop new Ta-type functional perovskites was to provide robust framework with good electrical transport properties different energy storage/conversion applications. To achieve this target, we conduct an extensive survey of BVS mismatch maps on both structure types (i.e., *P-3m1* and *Fm-3m*) to evaluate their diffusion behavior of H^+ and O^{2-} ions, as shown in Figure 6. Such a methodology was pioneered by Adams and others on various ionic conductors.[12, 62, 63] This could be helpful to select best candidates to further evaluate the for a number of potential applications, such as high temperature steam electrolysis, H-conducting solid oxide fuel cells and M-O_2 batteries.

As shown in Figure 6 with the projection on (110) and (100) planes, the above two space groups appear to have 3D-diffusion pathways for all investigated ions. Nonetheless, the smallest BVS mismatch values (unit valence; u.v.) to create to a continuous pathway vary considerably. For both *P-3m1* and *Fm-3m*, the lowest energy pathways could be obtained are for H^+ and O^{2-}, with 0.1 and 0.5 u.v., respectively. This is in good agreement with many acceptor-doped complex perovskites, for instance *Fm-3m* type $Ba_3Ca_{1.18}Nb_{1.82}O_{8.73}$, which show modest O^{2-} and H^+ conductivities, in dry air and humidified air, respectively, at elevated temperatures.[8] Up to now, no *P-3m1*-type perovskites with a general formula of $Ba_3M'_{1+x}M''_{2-x}O_{9-3x/2}$ ($0 \leq x \leq 0.5$; M' = divalent cations, M'' = penta-valent cations) have been reported to show protonic conduction. However, our result supports that such a crystal phase could be synthesized as a pure phase at relatively low temperature of 1000 °C. In practice, this type of compounds require advanced preparation techniques, such as pulsed laser deposition (PLD), to densify without using high temperature sintering.

Furthermore, we also consider the supercell configuration for compounds with different space groups, namely *Pm-3m*, *P3m1* and *Fm-3m*. This can allow us to understand the relative energies of different configurations when each atom is only allowed to fully occupy a single crystallographic site in the supercell structure. One important implication of such analysis is clustering of certain atoms in the unit cells and its impact on the local diffusion behavior. Instead of studying the whole $Ba_3Ca_{1+x}Ta_{2-x}O_{9-3x/2}$ series, $Ba_3Ca_{1.18}Ta_{1.82}O_{8.73}$ was selected as a case study because this composition can crystallize into different polymorphs in the investigated temperature range. For *Pm-3m*, 3x3x3 supercells were computed in which 27 crystallographic distinct positions were available for individual Ca and Ta ions. The total number of combinations was ca. 5×10^6. For *P3m1*, 3x3x2 supercells were computed in which 12 and 24 crystallographic distinct positions

were available for individual Ca and Ta ions to occupancy. The total number of combinations was

ca. 6.5×10^{10}. For *Fm-3m*, 2x2x2 supercells were computed in which 32 crystallographic distinct

positions were available for individual Ca and Ta ions to occupancy. The total number of

combinations was ca. 9.1×10^5. To handle such large number of supercell combination, the

columbic energies of all supercell combinations were as a selection rule. Only the 100 lowest

columbic energy combinations were output to investigate the thermodynamic local configurations.

All crystallographically equivalent supercells were automatically merged.

For the investigated lowest columbic energy supercells, we summarize the cationic

clustering effect as following. For the 3x3x3 supercell using *Pm-3m* cif file as the input, Ta_4Ca_3

clusters was found to be the most favorable local configurations, together with the less favorable

local configurations of Ta_6Ca. All the clusters have an interatomic distance of ca. 4.17 Å. For the

3x2x2 supercell using *P-3m1* cif file as the input, Ta_4Ca_3 and Ta_5Ca_2 clusters were found to be the

most favorable local configurations, together with the less favorable local configurations of Ta_6Ca,

Ta_3Ca_4 and Ta_2Ca_5. All the clusters have interatomic distances in the range of 4.16 - 4.25 Å. For

the 2x2x2 supercell of the *Fm-3m* structure, Ta_2Ca_5 clusters was found to be the most favorable

local configurations, together with the less favorable local configurations of Ta_7, $TaCa_6$ and Ta_3Ca_4.

All of the clusters have an interatomic distance of ca. 4.21 Å.

Bond valence energy landscape (BVEL) calculations were further used to illustrate the

impact of local ordering on the oxide-ion diffusion pathway. As shown in Figure 7, the diffusion

pathway for oxide-ion was not equivalent around the CaO_6 and TaO_6 octahedra environments in

all investigated supercells generated from *Pm-3m*, *P-3m1* and *Fm-3m* cif files. The oxide ions are

more efficient to hop when two TaO_6 octahedra are corner connected with each other, as part of

the clustering described above. In addition, oxide-ion vacancy was more energetically stable to

form in CaO_6 octahedra. As the Ca^{2+} ions are less positively charged compared to Ta^{5+} ions in MO_6 octahedra, therefore, smaller amount of enthalpy is required to overcome the coulombic energy upon the formation of MO_5 polyhedra during oxide-ion vacancy formation in the structures.

3.3 Microstructure effect and Electrical Conductivity Analysis. The impact of chemical compositions and atmospheres on the conductivity was systematically analyzed through ISGP. Nonstoichiometric compositions with x > 0 exhibit an increase in conductivity in comparison to the stoichiometric composition with x = 0. The electrical conductivity under air atmosphere increases with the x content up to the end member BCT36. As the x (Ca^{2+}) amount is increased, concentration of oxide ion vacancies and hence the oxide ion conductivity also increase (Equation 3).

$$3O_O^x + 2CaO + 2Ta_{Ta}^x \rightarrow 3Ca_{Ta}''' + 3V_{\ddot{O}} + Ta_2O_5$$

[3]
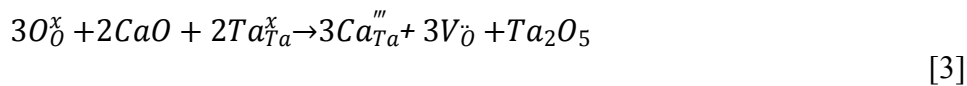
A very low concentration of mobile charge carriers is indicated by the small pre-exponential term A for BCT00, as shown in Table 2. However, in 3% H_2O/Air, 3% D_2O/air, and N_2 atmospheres, conductivity increased up to x= 0.27 and then decreased when x reached to 0.36. In 3% H_2O/Air, 3% D_2O/air, and N_2 atmospheres, apart from oxide ion conductivity, protonic (H^+/D^+), and h• charge carriers also take part in the transport process, according to Equations [4] and [5]:

$$H_2O_{(g)} + V_{\ddot{O}(s)} + O_O^x \rightarrow 2OH_{O(s)}^{\cdot}$$

[4]

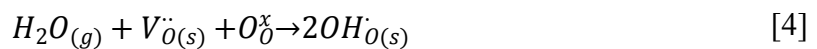$$V_{\ddot{O}(s)} + 0.5O_2 \leftrightarrow O_{O(s)}^x + 2h^{\cdot}$$

[5]

Table 2 shows that the decrease in pre-exponential factor after BCT27 indicates that a decrease in concentration of free charge carriers was the major contributing factor for the decrease in conductivity. It is safe to assume that charge compensating $V_{\ddot{O}}$ defect produced due to Ca doping at Ta site (Ca_{Ta}''') is equal to the concentration of excess Ca^{2+} ions (Equation 1). Hence, increase in

x (Ca^{2+}) leads to increase in $V_{\ddot{O}}$ concentration and hence the conductivity in ideal conditions. However, these oppositely charged defects are not always free or mobile. Depending on the composition and atmosphere, the similar relaxation times of electrochemical processes related to the bulk and GB transport in BCT were hard to separate through conventional ECM method and thus the EIS data of BCT samples in the temperature range of 300 - 800 °C under air, 3% H_2O/Air, N_2, and 3% D_2O/air atmospheres were analysed through ISGP.

Figure 8 and Figure S3 show the Nyquist plots of experimental data, while Figure 9a-d show the corresponding DFRT plots for all compositions under all atmospheres at 500°C, with fitted data obtained though ISGP analysis. In the DFRT plot, with the increasing order of relaxation time, the peaks could be assigned as P_{bulk}, P_{GB}, and $P_{electrode}$ contributions. The effective resistance of each relaxation process was analyzed from the area under the peak multiplied by the real part of impedance at lowest frequency. The out-of-range high frequency data corresponds to the series resistance plus other series resistances. Figure 9a-d illustrates the DFRT plots of BCT 18 as a representative between temperature ranges of 300 to 800 °C and contain three peaks in the studied frequency range. The corresponding capacitance, resistance values and relaxation times under all atmospheres for all compositions are summarized in Table 1. Figure 8a-d shows the Arrhenius plots of the total, bulk, grain boundary conductivity values under air, 3% H_2O/Air, 3% D_2O/air, and N_2 atmospheres for the BCT series.

The following possibilities can explain the decrease in electrical conductivity for x > 0.27 in 3% H_2O/Air, 3% D_2O/air, and N_2 atmospheres: (i) formation of defect associates such as $[V_{\ddot{O}} Ca_{Ta}'' V_{\ddot{O}}]^x$ with increase in x, as increase in x content leads to increase in effective negative Ca_{Ta}'' defects, which can trap the positive defects such as $V_{\ddot{O}}$, H^+ and $h^{\cdot}$, making them immobile; (ii) non-availaiblity of $V_{\ddot{O}}$ defects for proton and oxide conduction due to $V_{\ddot{O}}$ ordering. Highest pre-

exponential term for BCT36 under H_2O/Air, 3% D_2O/air, and N_2, support this hypothesis (Table 2). The increase in electrical conductivity with x in air atmosphere indicates that influence of clustering effect is dependent on the size of the mobile ions, as clustering effect is not affecting mobility of oxide ions, when compared to mobility of H^+/D^+. In all the cases, the lowest conductivity is seen in N_2 atmosphere which is low in oxygen and thus indicates presence of *p-type* charge carriers. It should be noted for the BCT series is that only BCT18/BCT27 show increase in conductivity in 3% H_2O/Air when compared to dry air. This indicates that the clustering effect is *pO_2* dependent.

Figure 10 shows presence of two/three regions of transport under all atmospheres with dominant proton transport in region I (T <500 °C), possible mixed conductivity (H^+/O^{2-}) around 450-550 °C, region II (T > 550 °C) by an O^{2-}/$h^{\cdot}$ conductivity. The activation energy remains almost constant under all atmospheres with an increase in x (Table 2). With an increase in x, we also see a simultaneous increase in activation energy related to bulk and grain-boundary processes, again, suggesting that decrease in conductivity after BCT27 is due to a decrease in the concentration of free charge carriers. Lastly, we also examined the effect of x on the apparent density. Figure S1 shows the microstructure of the sintered pellets after conductivity measurements. It is readily apparent from the SEM images that with an increasing Ca/Ta ratio, there is an increase in grain size and decrease in porosity as CaO is acting as a sintering aid. The relative density was also found to increase with an increase in the Ca/Ta ratio.

4. CONCLUSIONS

In current report, the structural and transport properties of $Ba_3Ca_{1+x}Ta_{2-x}O_{9-3x/2}$ ($0 \leq x \leq 0.36$) were evaluated between 1000 and 1550 °C. For the first time, the single phase *Fm-3m*

$Ba_3Ca_{1+x}Ta_{2-x}O_{9-3x/2}$ ($0.09 \leq x \leq 0.36$) oxides were synthesized at 1550 °C. However, $Ba_3CaTa_2O_9$ crystallized in *P-3m1* phase between 1000 and 1550 °C. BVS analysis suggests that the investigated samples should have interesting transport behaviors of various cations and anions. As such, they might be suitable for applying as functional oxides in energy storage/conversion systems. The *P-3m1* phases were shown to possess interesting CO_2 absorption property. The electrical conductivity increased from $x = 0$ to $x = 0.27$ and then decreased for end member $x = 0.36$ due to decrease in mobile charge carriers in all atmospheres except in air. Interestingly, in dry air, electrical conductivity increased from $x = 0$ to $x = 0.36$, indicating that defect associate. Additionally, only BCT18/BCT27 showed increase in conductivity in humid atmospheres, which indicates that the clustering effect was *pO_2* dependent.

REFERENCES

1. H. Iwahara, T. Esaka, H. Uchida, N. Maeda, Proton conduction in sintered oxides and its application to steam electrolysis for hydrogen production, *Solid State Ionics,* 1981, **3-4**, 359-363.

2. K. C. Liang, Y. Du, A. S Nowick, Fast high-temperature proton transport in nonstoichiometric mixed perovskites, *Solid State Ionics,* 1994, **69 (2)**, 117-120.

3. Y. Du, A. S. Nowick, Structural transitions and proton conduction in nonstoichiometric $A_3B'B''O_9$ perovskite-type oxides, *Journal of the American Ceramic Society,* 1995, **78 (11)**, 3033-3039.

4. A. S. Nowick, Y. Du, K. C. Liang, Some factors that determine proton conductivity in nonstoichiometric complex perovskites, *Solid State Ionics,* 1999, **125 (1)**, 303-311.

5. W. H. Kan, T. T. Trinh, T. Fürstenhaupt, V. Thangadurai, Synthesis, rietveld refinement of crystal structure, electron diffraction, and electrical transport properties of $Ba_2(Ca_{1-x-y}Fe_xNb_y)(Nb_{1-z}Fe_z)O_{6-\delta}$ double perovskites, *Canadian Journal of Chemistry,* 2011, **89 (6)**, 688-696.

6. W. H. Kan, M. Roushanafshar, A. Vincent, T. Fürstenhaupt, M. Parvez, J. Luo, V. Thangadurai, Effect of substitution of B-sites by Mn, Fe and Co in double perovskite-type $Ba_3CaNb_2O_9$ on structure and electrical properties, *RSC Advances*, 2013, **3 (45)**, 23824-23832.

7. W. H. Kan, P. Dong, J.-S. Bae, S. Adams, V. Thangadurai, Probing surface valence, magnetic property, and oxide ion diffusion pathway in B-site ordered perovskite-type $Ba_2Ca_{0.67}M_{0.33}NbO_{6-\delta}$ (M=Mn, Fe, Co) , *Solid State Ionics,* 2016, **290,** 90-97.

8. K. Singh, W. H. Kan, B. Patton, A. Huq, V. Thangadurai, Insights into B-Site ordering in double perovskite-type $Ba_3Ca_{1+x}Nb_{2-x}O_{9-\delta}$ ($0 \leq x \leq 0.45$): Combined synchrotron and neutron diffraction and electrical transport analyses, *Inorganic Chemistry*, 2018, **57 (5)**, 2609-2619.

9. R. Shannon, Revised effective ionic radii and systematic studies of interatomic distances in halides and chalcogenides, *Acta Crystallographica Section A*, 1976, **32 (5)**, 751-767.

10. P. Vanýsek, Electrochemical Series. In CRC Handbook of Chemistry and Physics. 77th ed.; D. R. Lide, H. P. R. Frederikse, Eds. Chemical Rubber Publishing Company: Boca Raton: 1996; pp 8-20– 8-30.

11. V. Thangadurai, H. Kaack, W. J. F. Weppner, Novel fast lithium ion conduction in garnet-type $Li_5La_3M_2O_{12}$ (M = Nb, Ta), *Journal of the American Ceramic Society*, 2003, **86 (3)**, 437-440.

12. V. Thangadurai, S. Adams, W. Weppner, Crystal structure revision and identification of li$^+$-ion migration pathways in the garnet-like $Li_5La_3M_2O_{12}$ (M = Nb, Ta) oxides, *Chemistry of Materials*, 2004, **16 (16)**, 2998-3006.

13. W. H. Kan, D. Chen, J. K. Papp, A. K. Shukla, A. Huq, C. M. Brown, B. D. McCloskey, G. Chen, Unravelling solid-state redox chemistry in $Li_{1.3}Nb_{0.3}Mn_{0.4}O_2$ single-crystal cathode material, *Chemistry of Materials*, 2018, **30 (5)**, 1655-1666.

14. W. H. Kan, B. Deng, Y. Xu, A. K. Shukla, T. Bo, S. Zhang, J. Liu, P. Pianetta, B.-T.Wang, Y. Liu, G. Chen, Understanding the effect of local short-range ordering on lithium diffusion in $Li_{1.3}Nb_{0.3}Mn_{0.4}O_2$ single-crystal cathode, *Chem*, 2018, **4 (9)**, 2108-2123.

15. W. H. Kan, C. Wei, D. Chen, T. Bo, B.-T.Wang, Y. Zhang, Y. Tian, J.-S. Lee, Y. Liu, G. Chen, Evolution of local structural ordering and chemical distribution upon delithiation of

a rock salt–structured $Li_{1.3}Ta_{0.3}Mn_{0.4}O_2$ cathode, *Advanced Functional Materials*, 2019, **29 (17)**, 1808294.

16. V. P. Filonenko, I. P. Zibrov, High-pressure phase transitions of M_2O_5 (M = V, Nb, Ta) and thermal stability of new polymorphs, *Inorganic Materials*, 2001, **37 (9)**, 953-959.

17. B. Kennedy, P. Saines, Y. Kubota, C. Minakata, H. Hano, K. Kato, M. Takata, Crystal structures and phase transitions in Ba_2HoTaO_6, *Materials Research Bulletin*, 2007, **42 (11)**, 1875-1880.

18. P. J. Saines, J. R. Spencer, B. J. Kennedy, M. Avdeev, Structures and crystal chemistry of the double perovskites $Ba_2LnB'O_6$ (Ln=lanthanide $B'=Nb^{5+}$ and Ta^{5+}): Part I. Investigation of Ba_2LnTaO_6 using synchrotron X-ray and neutron powder diffraction, *Journal of Solid State Chemistry*, 2007, **180 (11)**, 2991-3000.

19. M. W. Lufaso, R. B. Macquart, Y. Lee, T. Vogt, H.-C. zur Loye, Pressure induced octahedral tilting distortion in Ba_2YTaO_6, *Chemical Communications*, 2006, **37**, 168-170.

20. Q. Zhou, B. J. Kennedy, J. A. Kimpton, The effect of disorder in Ba_2YTaO_6 on the tetragonal to cubic phase transition, *Journal of Solid State Chemistry*, 2011, **184 (4)**, 729-734.

21. K. S. Wallwork, B. J. Kennedy, Q. Zhou, Y. Lee, T. Vogt, Pressure and temperature-dependent structural studies of Ba_2BiTaO_6, *Journal of Solid State Chemistry*, 2005, **178 (1)**, 207-211.

22. Q. Zhou, P. Blanchard, B. J. Kennedy, E. Reynolds, Z. Zhang, W. Miiller, J. B. Aitken, M. Avdeev, L.-Y. Jang, J. A. Kimpton, Synthesis, structural and magnetic studies of the double perovskites Ba_2CeMO_6 (M = Ta, Nb), *Chemistry of Materials*, 2012, **24 (15)**, 2978-2986.

22

23. P. Kumari, A. Dutta, S. Shannigrahi, S. Prasad, T. P. Sinha, Electronic structure and electrical properties of Ba_2LaTaO_6, *Journal of Alloys and Compounds*, 2014, **593**, 275-282.

24. Y. Doi, Y. Hinatsu, Magnetic properties of ordered perovskites Ba_2LnTaO_6 (Ln = Y, lanthanides), *Journal of Physics: Condensed Matter*, 2001, **13 (19)**, 4191-4202.

25. Q. Zhou, B. J. Kennedy, High temperature structural studies of Ba_2BiTaO_6, *Solid State Sciences*, 2005, **7 (3)**, 287-291.

26. J.-H. Choy, S.-T. Hong, J.-H. Park, D.-K. Kim, Crystal Structure and the role of covalency in eight-layered hexagonal Ba_2CrTaO_6, *Japanese Journal of Applied Physics*, 1993, **32 (Part 1, No. 10)**, 4628-4634.

27. S. K.-Sack, I. Thumm, M. Herrmann, Über Verbindungen vom Typ $Ba_3B^{II}MO_9$ mit B^{II} □ Mg, Ca, Sr, Ba und M^V □ Nb, Ta, *Zeitschrift für anorganische und allgemeine Chemie*, 1981, **479 (8)**, 177-183.

28. B. M. Collins, A. J. Jacobson, B. E. F. Fender, Preparation of the ordered perovskite-like compounds $Ba_4M_3LiO_{12}$ (M = Ta,Nb): A powder neutron diffraction determination of the structure of $Ba_4Ta_3LiO_{12}$, *Journal of Solid State Chemistry*, 1974, **10 (1)**, 29-35.

29. N. Taira, Y. Hinatsu, Magnetic susceptibility of Ba_2YbTaO_6 with the ordered perovskite structure and electron paramagnetic resonance of Yb^{3+} doped in Ba_2LuTaO_6, *Journal of Solid State Chemistry*, 2000, **150 (1)**, 31-35.

30. M. C. Verbraeken, H. A. L. Viana, P. Wormald, J. T. S. Irvine, A structural study of the proton conducting B-site ordered perovskite $Ba_3Ca_{1.18}Ta_{1.82}O_{8.73}$, *J. Phys. Condens. Matter*, 2011, **23 (23)**, 234111.

31. D. Rout, G. B. Santosh, V. Subramanian, V. Sivasubramanian, Study of cation ordering in Ba(Yb$_{1/2}$Ta$_{1/2}$)O$_3$ by X-ray diffraction and raman spectroscopy, *International Journal of Applied Ceramic Technology,* 2008, **5 (5)**, 522-528.

32. T. S. Hammink, W. T. Fu, D. J. W. Ijdo, Crystal structure of Ba$_2$InTaO$_6$ as determined by the rietveld refinement, *Journal of Solid State Chemistry,* 2011, **184 (4)**, 848-851.

33. J. Srinivas, E. D. Dias, G.M. Sreenivasa, Crystal structure of Ba(Mg$_{1/3}$Ta$_{2/3}$)O$_3$ calcinated at 1400°C, *Bulletin of Materials Science,* 1997, **20 (1)**, 23-25.

34. S. Janaswamy, G. M. Sreenivasa, E. D. Dias, V. R. K. Murthy, Structural analysis of BaMg$_{1/3}$(Ta,Nb)$_{2/3}$O$_3$ ceramics, *Materials Letters,* 2002, **55 (6)**, 414-419.

35. L. Padel, P. Poix, J. C. Bernier, A. Michel, Structure et proprietes magnetiques de la perovskite Ba$_2$TaCoO$_6$, *Materials Research Bulletin,* 1972, **7 (5)**, 443-448.

36. V. Filip'ev, E. Fesenko, Preparation and unit-cell parameters of Ä2ÇIBIIO6 compounds, *Kristallografiya,* 1961, **6 (5)**, 770-772.

37. A. Agranovskaya, Physical-chemical investigation of the formation of complex ferroelectrics with the perovskite structure, *Bull. Acad. Sci. USSR Ser. Phys,* 1960, **24,** 1271-1277.

38. I. M. Reaney, P. L. Wise, I. Qazi, C. A. Miller, T. J. Price, D. S. Cannell, D. M. Iddles, M. J. Rosseinsky, S. M. Moussa, M. Bieringer, L. D. Noailles, R. M. Ibberson, Ordering and quality factor in 0.95BaZn$_{1/3}$Ta$_{2/3}$O$_3$–0.05SrGa$_{1/2}$Ta$_{1/2}$O$_3$ production resonators, *Journal of the European Ceramic Society,* 2003, **23 (16)**, 3021-3034.

39. R. Mani, N. S. P. Bhuvanesh, K. V. Ramanujachary, W. Green, S. E. Lofland, J. Gopalakrishnan, A novel one-pot metathesis route for the synthesis of double perovskites,

$Ba_3MM'_2O_9$ (M = Mg, Ni, Zn; M'= Nb, Ta) with 1 : 2 ordering of M and M' atoms, *Journal of Materials Chemistry,* 2007, **17 (16)**, 1589-1592.

40. M. W. Lufaso, Crystal structures, modeling, and dielectric property relationships of 2:1 ordered $Ba_3MM'_2O_9$ (M = Mg, Ni, Zn; M' = Nb, Ta) perovskites, *Chemistry of Materials,* 2004, **16 (11)**, 2148-2156.

41. A. J. Jacobson, B. M. Collins, B. E. F. Fender, A powder neutron and X-ray diffraction determination of the structure of $Ba_3Ta_2ZnO_9$: an investigation of perovskite phases in the system Ba–Ta–Zn–O and the preparation of $Ba_2TaCdO_{5.5}$ and $Ba_2CeInO_{5.5}$, *Acta Crystallographica Section B,* 1976, **32 (4)**, 1083-1087.

42. F. Galasso, J. R. Barrante, L. Katz, Alkaline earth-tantalum-oxygen phases including the crystal structure of an ordered perovskite compound, $Ba_3SrTa_2O_9$, *Journal of the American Chemical Society,* 1961, **83 (13)**, 2830-2832.

43. H. Liu, S. Liu, V. Y. Zenou, C. Beach, N. Newman, Structural, dielectric, and optical properties of Ni-doped barium cadmium tantalate ceramics, *Japanese Journal of Applied Physics,* 2006, **45 (12)**, 9140-9142.

44. S. Asai, M. Soda, K. Kasatani, T. Ono, M. Avdeev, T. Masuda, Magnetic ordering of the buckled honeycomb lattice antiferromagnet Ba_2NiTeO_6, *Physical Review B,* 2016, **93 (2)**, 024412.

45. W. H. Kan, A. Huq, A. Manthiram, Low-temperature synthesis, structural characterization, and electrochemistry of Ni-rich spinel-like $LiNi_{2-y}MnyO_4$ (0.4 ≤ y ≤ 1), *Chemistry of Materials,* 2015, **27 (22)**, 7729-7733.

46. W. H. Kan, A. Huq, A. Manthiram, The first Fe-based Na^+-ion cathode with two distinct types of polyanions: $Fe_3P_5SiO_{19}$, *Chemical Communications,* 2015, **51 (52)**, 10447-10450.

47. W. H. Kan, A. Huq, A. Manthiram, Exploration of a metastable normal spinel phase diagram for the quaternary Li–Ni–Mn–Co–O system, *Chemistry of Materials,* 2016, **28 (6)**, 1832-1837.

48. W. H. Kan, S. Kuppan, L. Cheng, M. Doeff, J. Nanda, A. Huq, G. Chen, Crystal Chemistry and electrochemistry of $Li_xMn_{1.5}Ni_{0.5}O_4$ solid solution cathode materials, *Chemistry of Materials,* 2017, **29 (16)**, 6818-6828.

49. J. Liu, W. H. Kan, C. D. Ling, Insights into the high voltage layered oxide cathode materials in sodium-ion batteries: Structural evolution and anion redox, *Journal of Power Sources,* 2021, **481 (1)**, 229139.

50. D. Chen, W. H. Kan, G. Chen, Understanding performance degradation in cation-disordered rock-salt oxide cathodes, *Adv. Energy Mater.,* 2019, **9**, 1901255.

51. W. H. Kan, K-Y. Lai, A. Huq, A. Manthiram, Unravelling the low thermal expansion coefficient of cation-substituted $YBaCo_4O_{7+\delta}$, *Journal of Power Sources,* 2016, **307**, 454-461.

52. W. H. Kan, A. J. Samson, V. Thangadurai, Trends in electrode development for next generation solid oxide fuel cells, *J. Mater. Chem. A*, 2016, **4**, 17913-17932.

53. H. Schichlein, A. C. Müller, M. Voigts, A. Krügel, E. I. -Tiffée, Deconvolution of electrochemical impedance spectra for the identification of electrode reaction mechanisms in solid oxide fuel cells, *Journal of Applied Electrochemistry,* 2002, **32 (8)**, 875-882.

54. A. B. Tesler, D. R. Lewin, S. Baltianski, Y. Tsur, Analyzing results of impedance spectroscopy using novel evolutionary programming techniques, *Journal of Electroceramics,* 2010, **24 (4)**, 245-260.

55. S. Hershkovitz, S. Baltianski, Y. Tsur, Harnessing evolutionary programming for impedance spectroscopy analysis: A case study of mixed ionic-electronic conductors, *Solid State Ionics,* 2011, **188 (1)**, 104-109.

56. Z. Drach, S. Hershkovitz, D. Ferrero, P. Leone, A. Lanzini, M. Santarelli, Y. Tsur, Impedance spectroscopy analysis inspired by evolutionary programming as a diagnostic tool for SOEC and SOFC, *Solid State Ionics,* 2016, **288**, 307-310.

57. B. Toby, EXPGUI, a graphical user interface for GSAS, *Journal of Applied Crystallography,* 2001, **34 (2)**, 210-213.

58. M. Sale, M. Avdeev, 3DBVSMAPPER: A program for automatically generating bond-valence sum landscapes, *Journal of Applied Crystallography,* 2012, **45 (5)**, 1054-1056.

59. K. Okhotnikov, T. Charpentier, S. Cadars, Supercell program: a combinatorial structure-generation approach for the local-level modeling of atomic substitutions and partial occupancies in crystals, *Journal of Cheminformatics,* 2016, **8**, 17.

60. E. J. Abram, D. C. Sinclair, A. R. West, A Strategy for analysis and modelling of impedance spectroscopy data of electroceramics: Doped lanthanum gallate, *Journal of Electroceramics,* 2003, **10 (3)**, 165-177.

61. A. Borenstein, S. Hershkovitz, A. Oz, S. Luski, Y. Tsur, D. Aurbach, Use of 1,10-phenanthroline as an additive for high-performance supercapacitors, *The Journal of Physical Chemistry C,* 2015, **119 (22)**, 12165-12173.

62. S. Adams, Relationship between bond valence and bond softness of alkali halides and chalcogenides, *Acta Crystallographica Section B,* 2001, **57 (3)**, 278-287.

63. J. G.-Platas, C. G. Silgo, C. R.-Pérez, VALMAP 2.0: contour maps using the bond-valence-sum method, *Journal of Applied Crystallography,* 1999, **32 (2)**, 341-344.
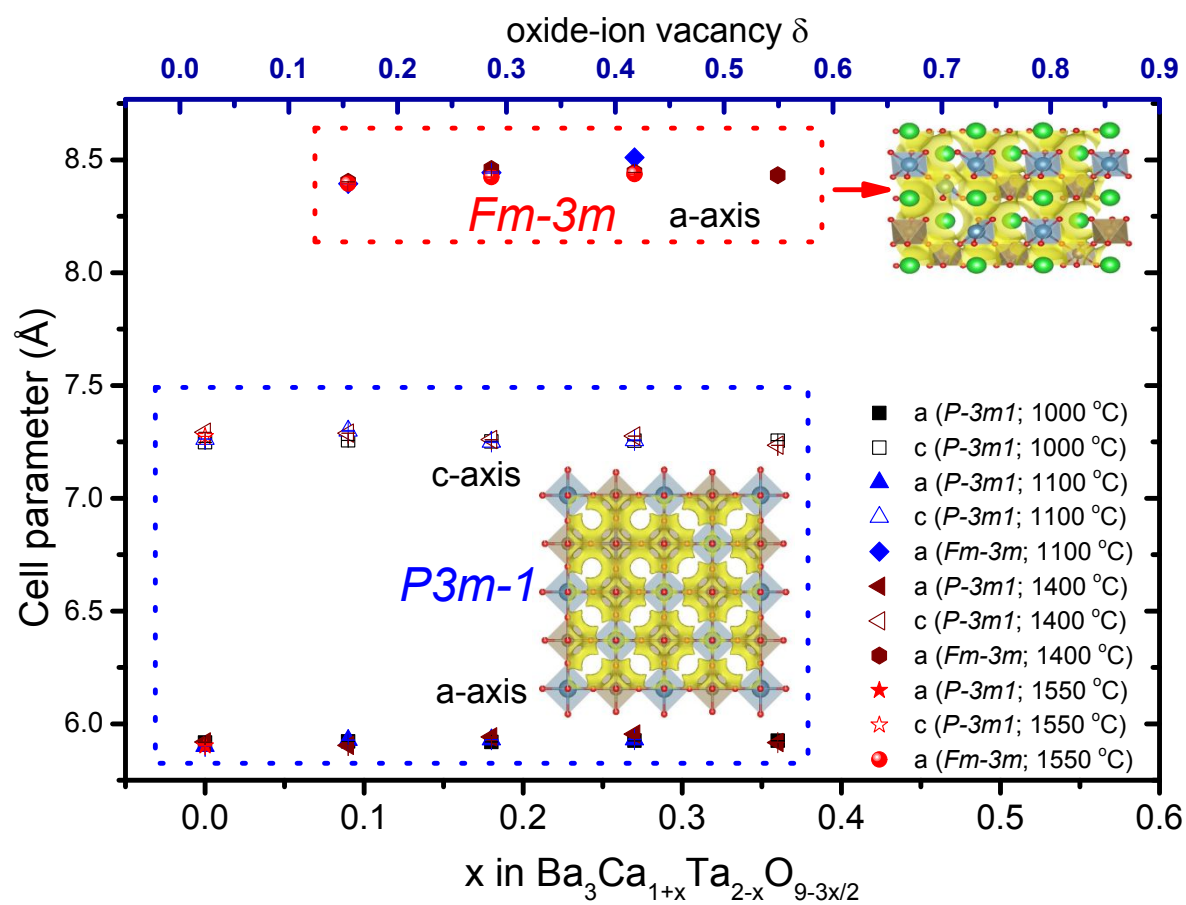
TOC

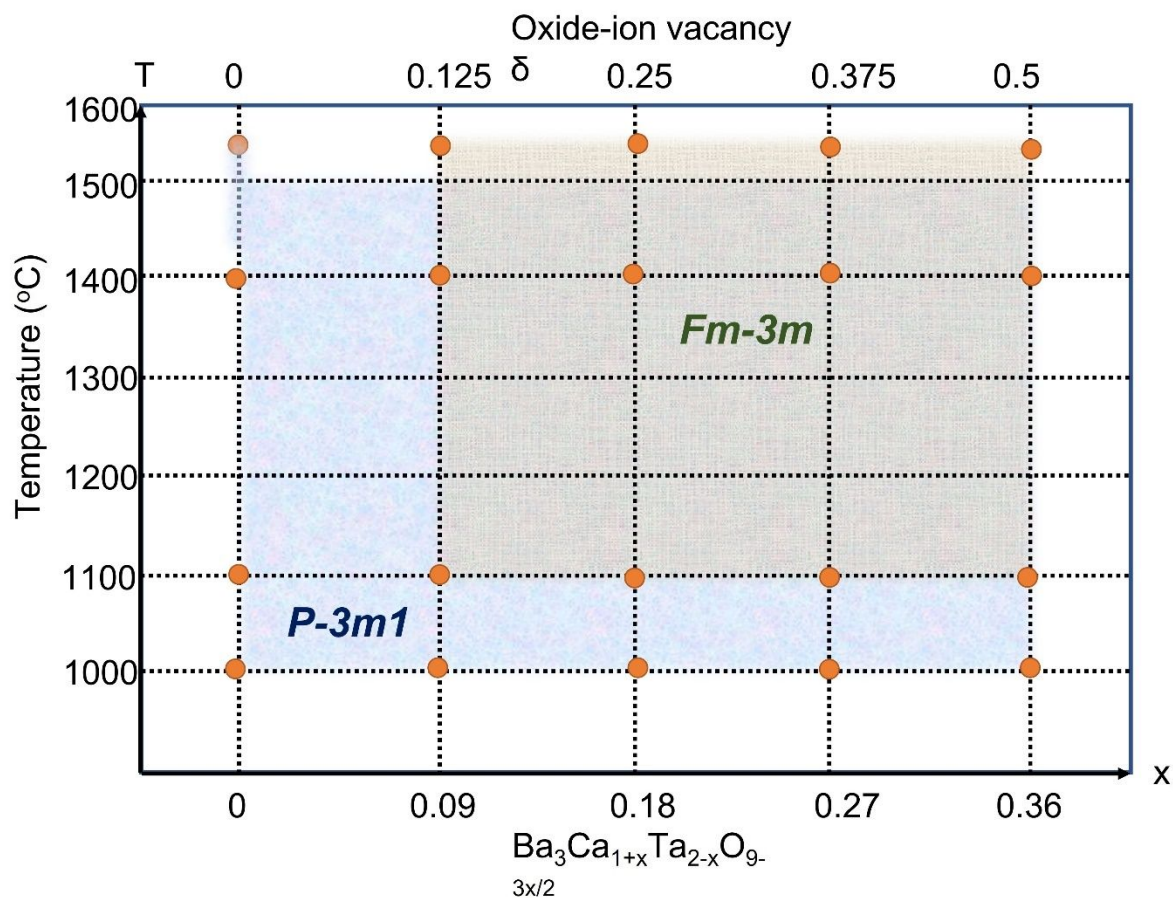Plot of cell parameter (Å) versus x in $Ba_3Ca_{1+x}Ta_{2-x}O_{9-3x/2}$ (bottom axis) and oxide-ion vacancy δ (top axis).

Legend:
- a (P-$3m1$; 1000 ^{o}C)
- c (P-$3m1$; 1000 ^{o}C)
- a (P-$3m1$; 1100 ^{o}C)
- c (P-$3m1$; 1100 ^{o}C)
- a (Fm-$3m$; 1100 ^{o}C)
- a (P-$3m1$; 1400 ^{o}C)
- c (P-$3m1$; 1400 ^{o}C)
- a (Fm-$3m$; 1400 ^{o}C)
- a (P-$3m1$; 1550 ^{o}C)
- c (P-$3m1$; 1550 ^{o}C)
- a (Fm-$3m$; 1550 ^{o}C)

Figure Caption

Figure 1. Functional phase diagram of $Ba_3Ca_{1+x}Ta_{2-x}O_{9-3x/2}$ ($0 \leq x \leq 0.36$) as a function of temperature and off-stoichiometry. The orange spots represent the exact experimental conditions being investigated in the current study.
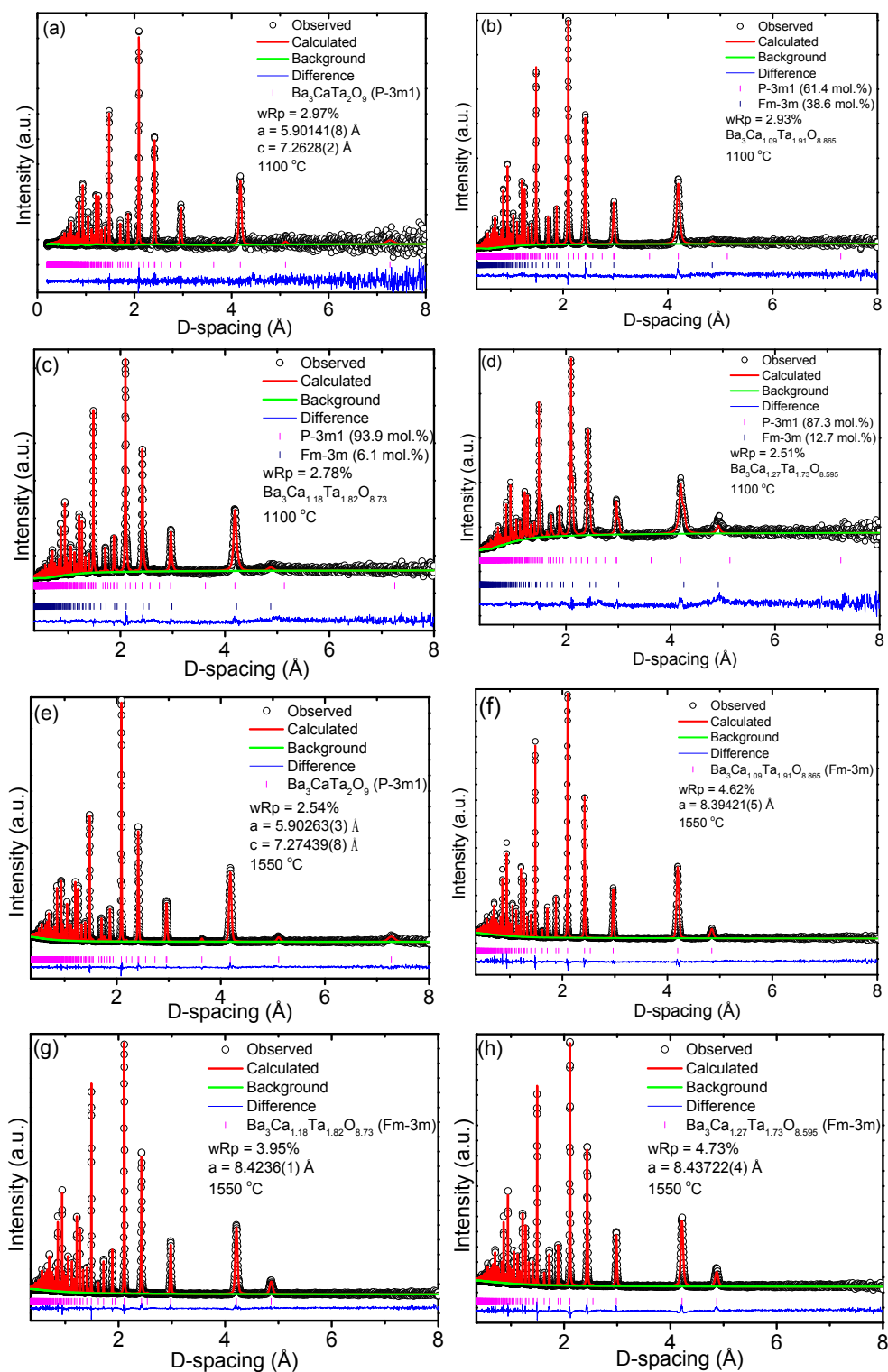
Figure 2. Rietveld refinement of TOF-Neutron diffraction data for $Ba_3Ca_{1+x}Ta_{2-x}O_{9-3x/2}$ ($0 \leq x \leq 0.27$). The samples were prepared at 1100 °C, (a-d) and 1550 °C (e-f).
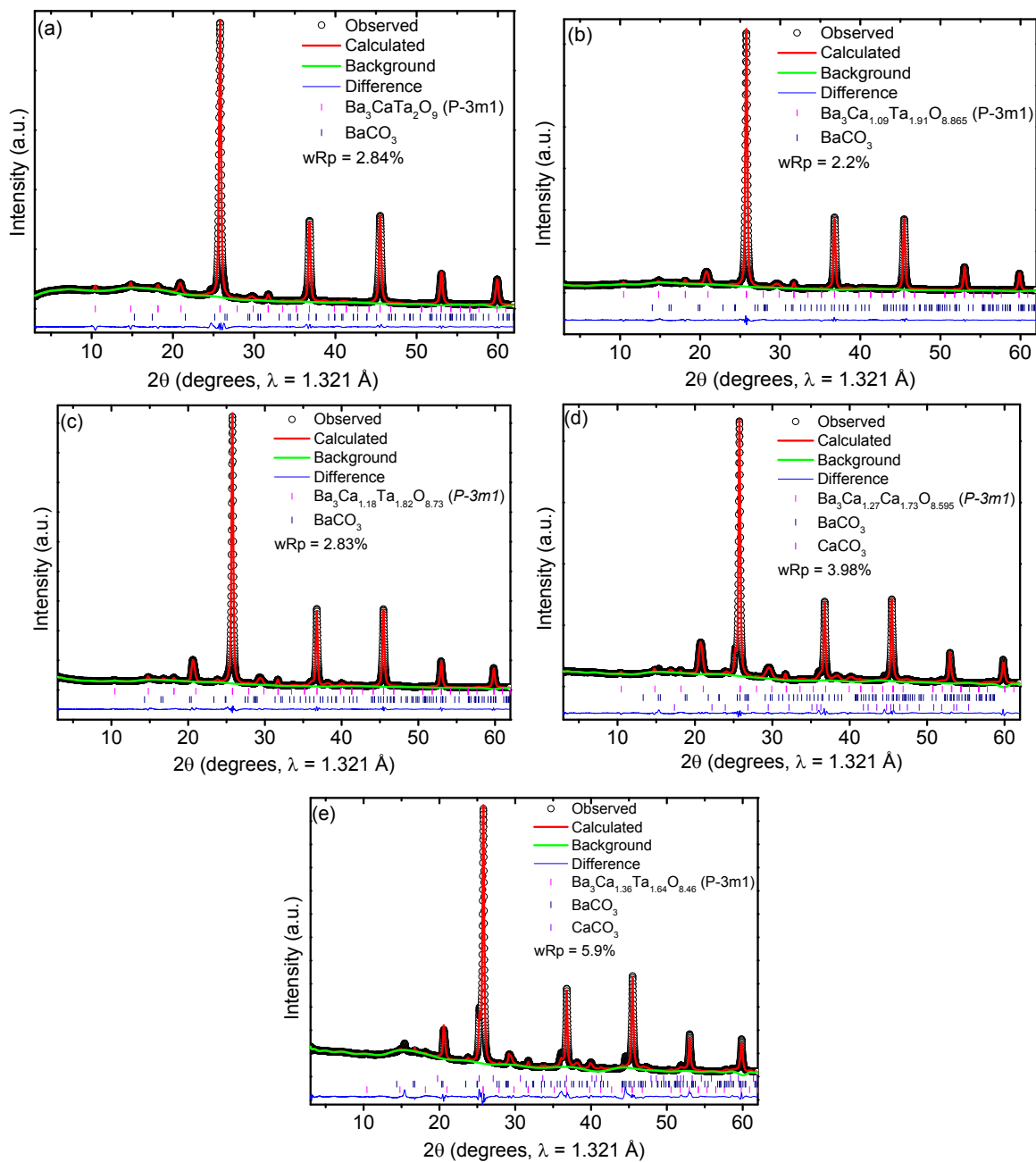
Figure 3. Rietveld refinement of monochromatic synchrotron X-ray diffraction data for $Ba_3Ca_{1+x}Ta_{2-x}O_{9-3x/2}$ ($0 \leq x \leq 0.36$). The samples were prepared at 1000 °C, (a-e).

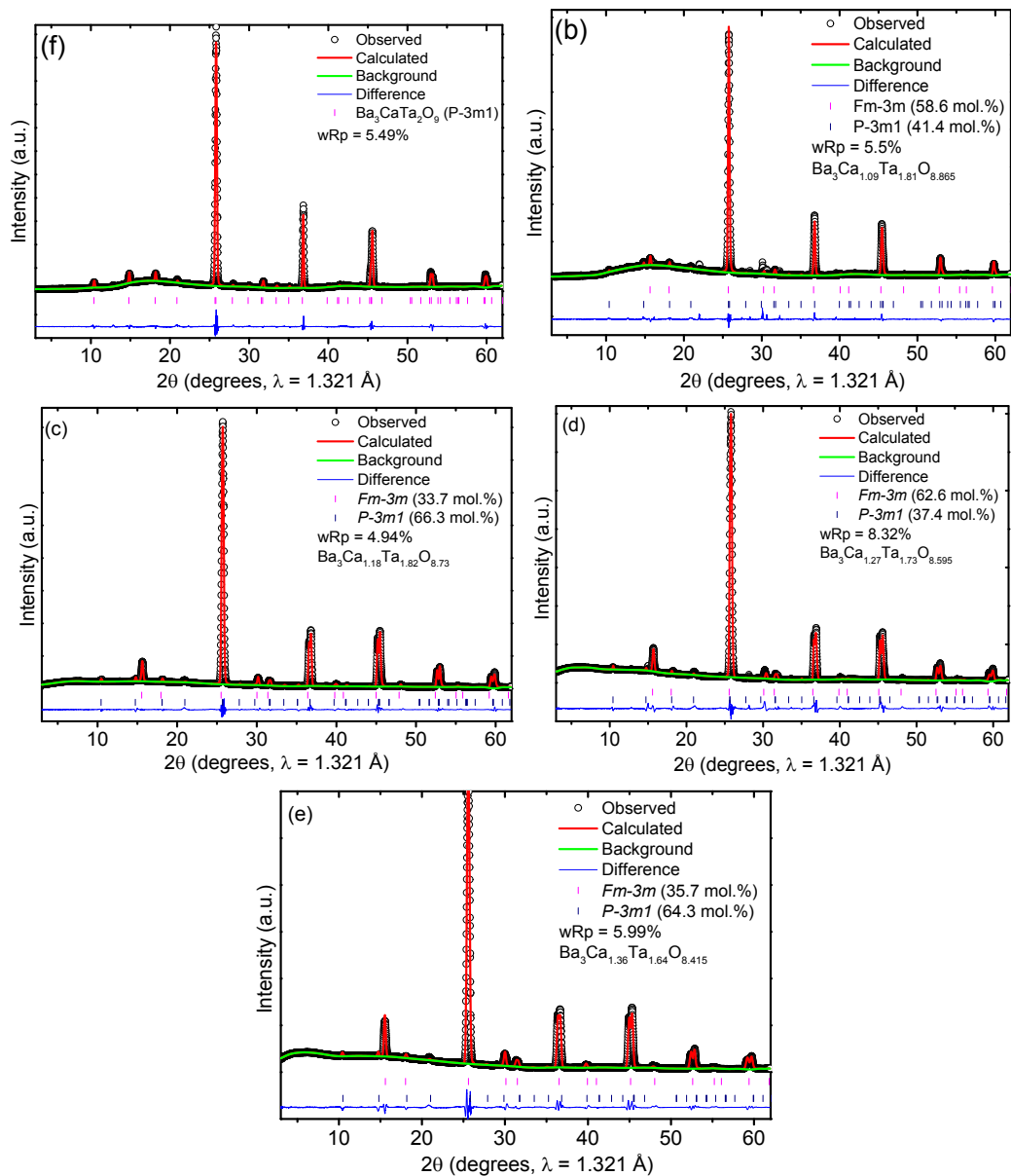**Figure 4.** Rietveld refinement of monochromatic synchrotron X-ray diffraction data for $Ba_3Ca_{1+x}Ta_{2-x}O_{9-3x/2}$ ($0 \leq x \leq 0.36$). The samples were prepared at 1400 °C (a-e).
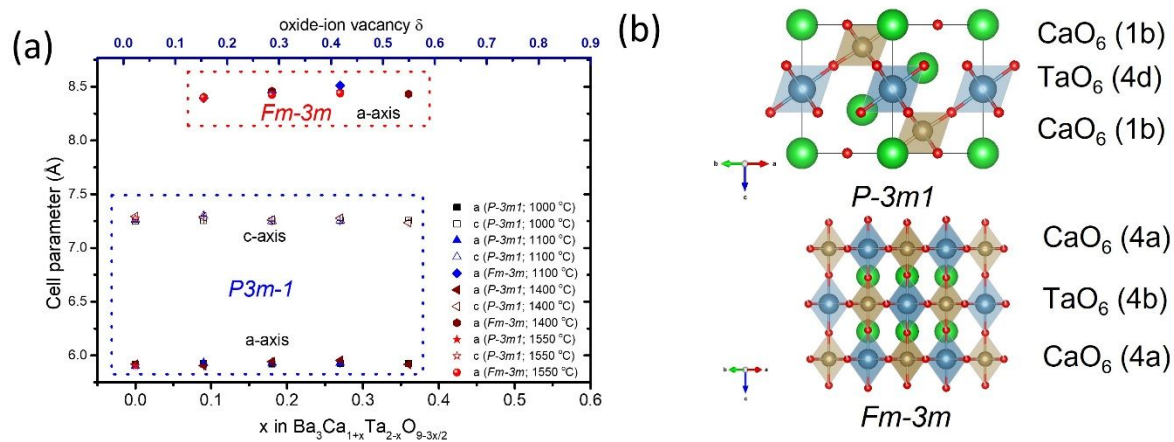
Figure 5. Structural analysis of *P-3m1* and *Fm-3m* phases as a function of temperature and stoichiometry: (a) Cell parameters, and (b) Crystal structures of *P-3m1* and *Fm-3m* phases.
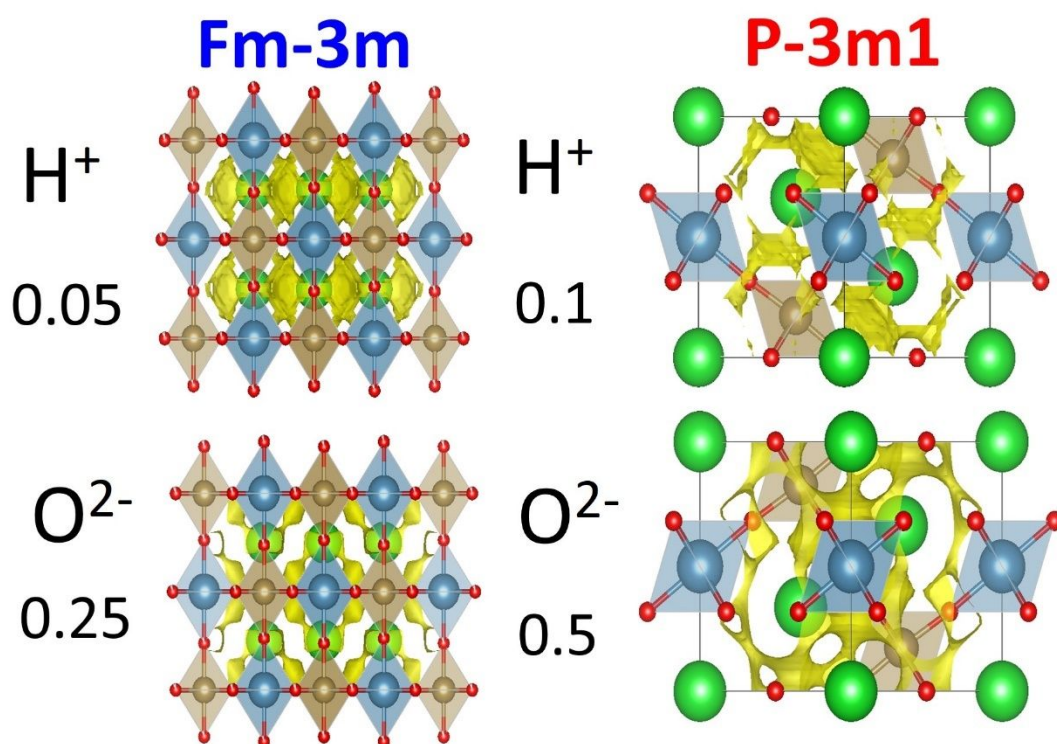
Figure 6. The bond valence sum (BVS) mismatch map calculation on *Fm-3m* and *P-3m1* space groups for H$^+$, and O^{2-} mobile ions on the projection of (110) plane.
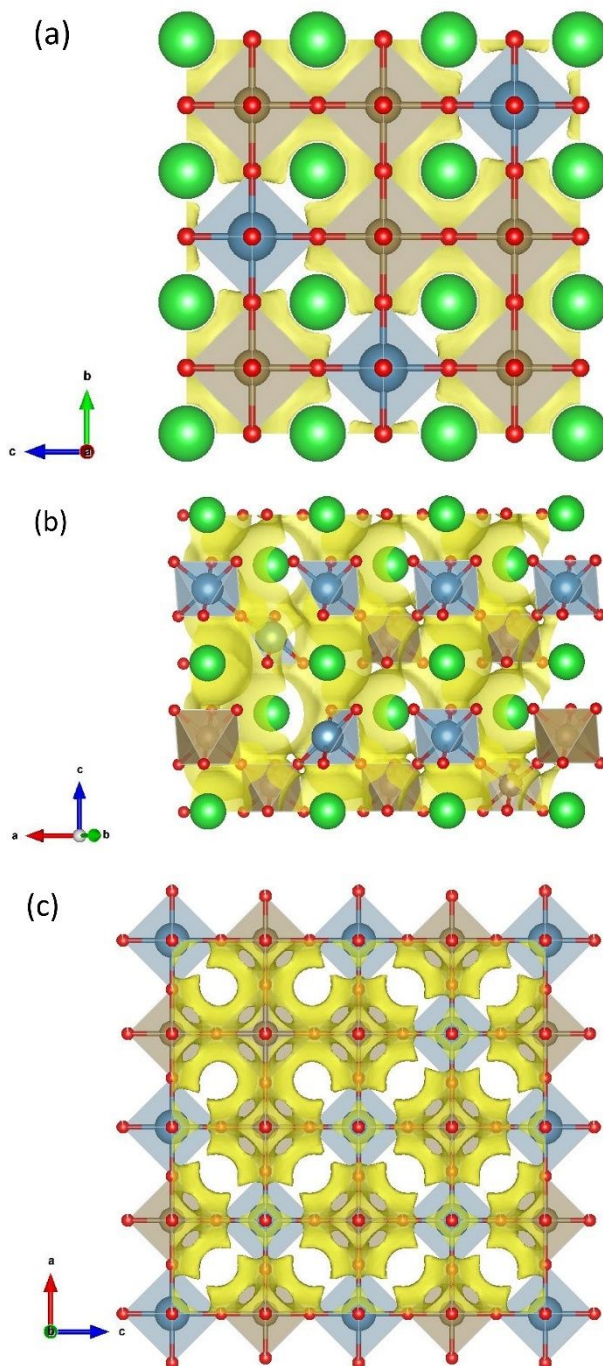
Figure 7. The bond valence energy landscape (BVEL) calculations for O^{2-} ions in the supercells generated from a) *Pm-3m*, b) *P-3m1* and c) *Fm-3m* as the input files. In (a), the projection of (100) plane was selected at x values between 0.25 and 0.5. In (b), the projection of (010) was selected at y values between 0.25 and 0.5. In (c), the projection of (010) was selected at y values between 0.2 and 0.35. Ba, Ca, Ta and O are represented by green, blue, brown and red spheres.
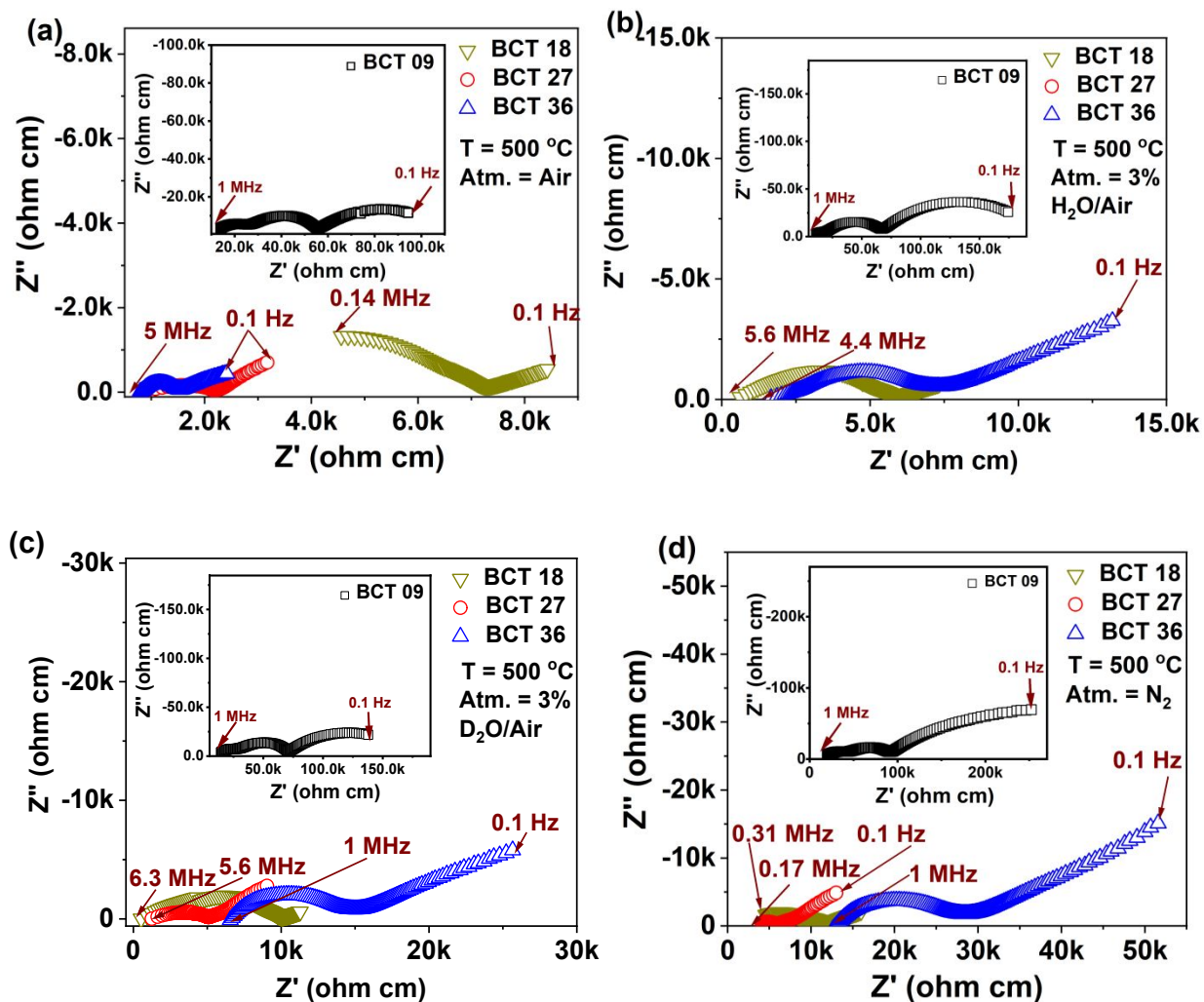
Figure 8. Nyquist plots at temperature 500 °C for $Ba_3Ca_{1.09}Ta_{1.91}O_{8.865}$ (BCT09), $Ba_3Ca_{1.18}Ta_{1.82}O_{8.73}$ (BCT18), $Ba_3Ca_{1.27}Ta_{1.73}O_{8.595}$ (BCT27), and $Ba_3Ca_{1.36}Ta_{1.64}O_{8.46}$ (BCT36) in (a) air, (b) 3%H_2O/air, (c) 3% D_2O/air, and (d) N_2.
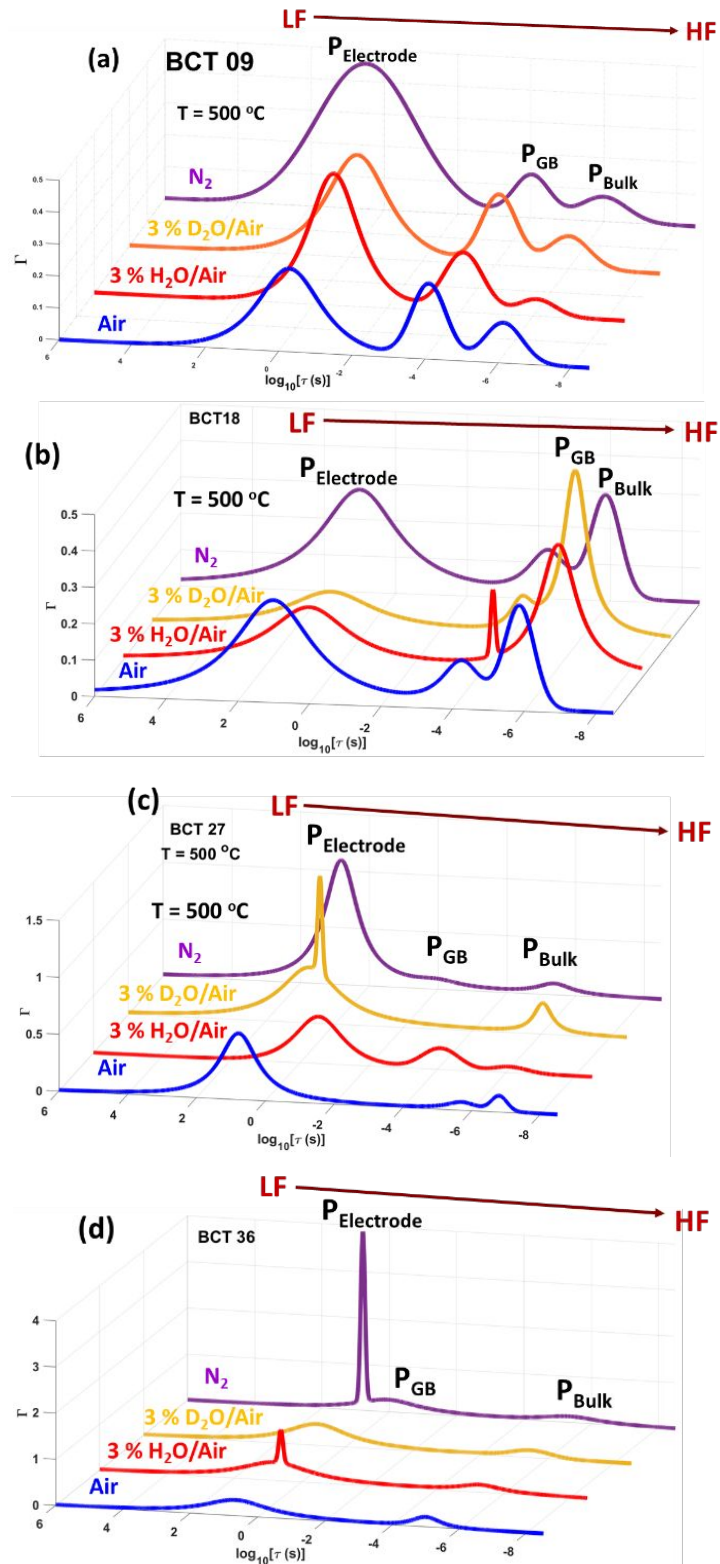
Figure 9. DFRT plots of (a) $Ba_3Ca_{1.91}Ta_{0.09}O_{9-3x/2}$ (BCT09), (b) $Ba_3Ca_{1.18}Ta_{1.82}O_{9-3x/2}$ (BCT18), (c) $Ba_3Ca_{1.27}Ta_{1.73}O_{9-3x/2}$ (BCT27), and (d) $Ba_3Ca_{1.36}Ta_{1.64}O_{9-3x/2}$ (BCT36) at 500 °C showing presence of three peaks due to bulk, grain-boundary (GB), and electrode transport processes.

Figure 10. Total, Bulk and grain boundary transport for (a) $Ba_3Ca_{1.91}Ta_{0.09}O_{9-3x/2}$ (BCT09), (b) $Ba_3Ca_{1.18}Ta_{1.82}O_{9-3x/2}$ (BCT18), (c) $Ba_3Ca_{1.27}Ta_{1.73}O_{9-3x/2}$ (BCT27), and (d) $Ba_3Ca_{1.36}Ta_{1.64}O_{9-3x/2}$ (BCT36).

Table 1. Fitting parameters of impedance plots for BCT samples in different temperatures and atmospheres.

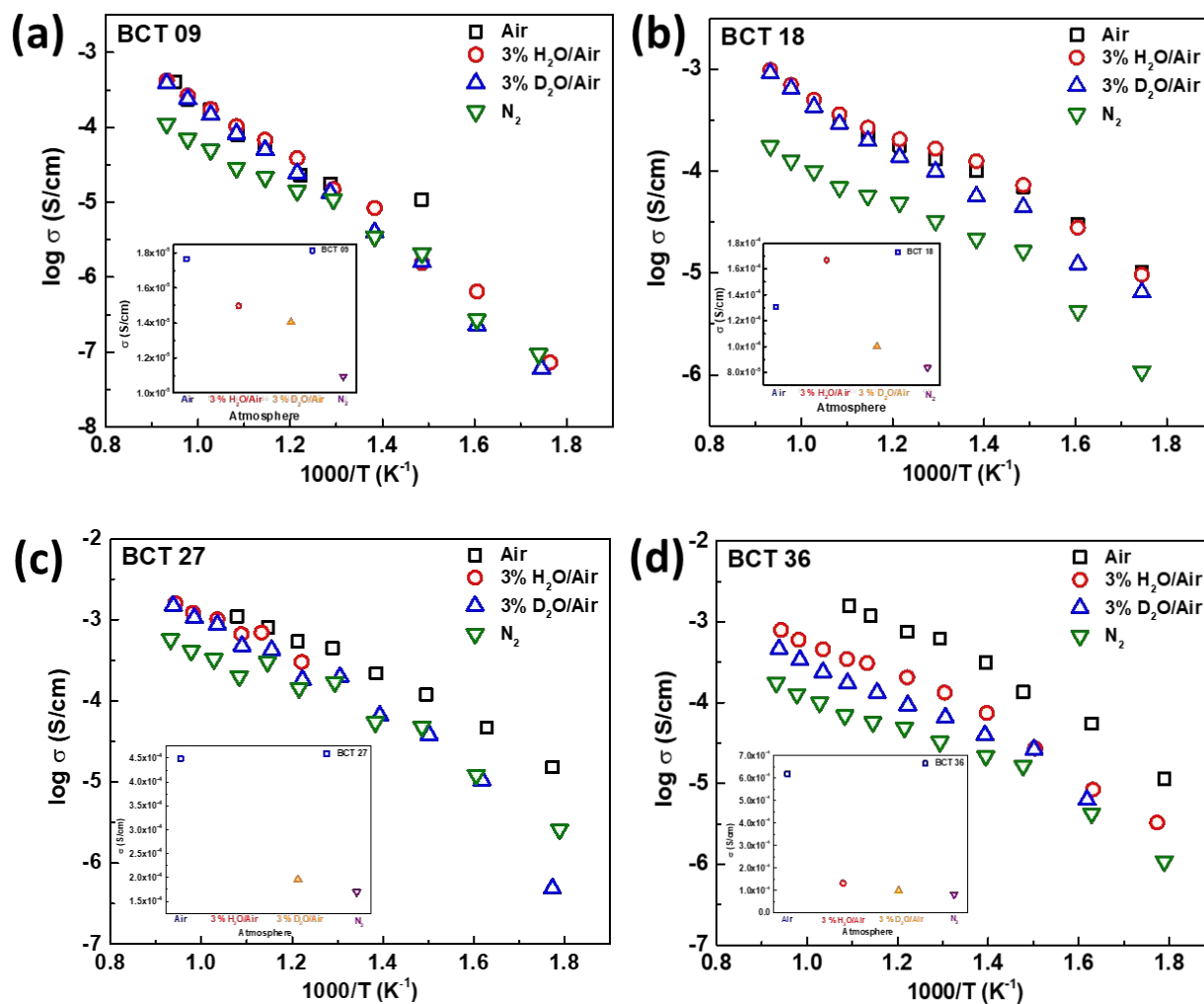| x	Rs (Ω)	R1 (Ω)	C1(F)	R2 (Ω)	C2 (F)	R3 (Ω)	C3 (F)
$Ba_3Ca_{1+x}Ta_{2-x}O_{9-\delta}$ (BCT) samples at 500 ºC under air							
0.09	3175	4069	1×10^{-10}	6838	1.1×10^{-8}	15359	3.25×10^{-5}
0.18	7929	9052	1×10^{-10}	3353	8×10^{-9}	13403	7.46×10^{-6}
0.27	226	40	4×10^{-9}	64	3×10^{-8}	665	8.89×10^{-3}
0.36	87	66	1.47×10^{-7}	346	1.28×10^{-2}	--	--

x	Rs (Ω)	R1 (Ω)	C1(F)	R2 (Ω)	C2 (F)	R3 (Ω)	C3 (F)
$Ba_3Ca_{1+x}Ta_{2-x}O_{9-\delta}$ (BCT) samples at 500 ºC under 3% H_2O/N_2							
0	1	1×10^5	0.003	--	--	--	--
0.09	2684	3063	1×10^{-10}	11316	7×10^{-9}	35942	7.94×10^{-6}
0.18	89	753	1×10^{-9}	33	1.43×10^{-6}	725	8.8×10^{-3}
0.27	2	0	0.01	2	0.030	191	0.01
0.36	157	556	9.00×10^{-9}	2321	2.65×10^{-3}	179	2.28×10^{-2}

x	Rs (Ω)	R1 (Ω)	C1(F)	R2 (Ω)	C2 (F)	R3 (Ω)	C3 (F)
$Ba_3Ca_{1+x}Ta_{2-x}O_{9-\delta}$ (BCT) samples at 500 ºC under 3% D_2O/N_2							
0	1	1×10^5	0.003	--	--	--	--
0.09	3311	3725	1×10^{-10}	6822	1.1×10^{-8}	27208	2.17×10^{-5}
0.18	400	986	2×10^{-9}	101	4.55×10^{-7}	760	1.31×10^{-4}
0.27	559	249	7×10^{-9}	2581	6.28×10^{-5}	55	2.439
0.36	675	205	7×10^{-9}	646	1.2×10^{-8}	4293	1.24×10^{-3}

x	Rs (Ω)	R1 (Ω)	C1(F)	R2 (Ω)	C2 (F)	R3 (Ω)	C3 (F)
$Ba_3Ca_{1+x}Ta_{2-x}O_{9-\delta}$ (BCT) samples at 500 ºC under N_2							
0	1	8184	1×10^{-10}	10917	9×10^{-9}	330	3.12×10^{-5}
0.09	330	1	1.20	108	2.00	203	1.46
0.18	438	685	2×10^{-9}	433	1.23×10^{-7}	2737	3.65×10^{-3}
0.27	550	377	1.1×10^{-8}	167	6.25×10^{-5}	191	0.01
0.36	1184	1718	3×10^{-9}	5587	2.0×10^{-4}	4508	1.46×10^{-3}

Table 2. Activation Energy (Ea) and Pre-Exponential Term (A) for BCT (x = 0−0.36) under air, 3% H₂O/air, 3% D₂O/air, and N₂.

x	Air	3% H_2O/N_2	3% D_2O/N_2	N_2
	Ea (eV)	Ea (eV)	Ea (eV)	Ea (eV)
0.09	0.80	0.87	0.92	0.93 0.62
0.18	0.55 0.47	0.62 0.52	0.70 0.52	0.52
0.27	0.59 0.55	0.48	0.60	0.42
0.36	0.68 0.48	0.48 0.42	0.42	0.56 0.64